# Analysis of space-time correlations to support the development of wall-modeled LES

M. Boxho[1,4*], M. Rasquin[1], T. Toulorge[1], G. Dergham[2], G. Winckelmans[3] and K. Hillewaert[1,4]

[1*]Cenaero, Charleroi, 6041, Belgium.
[2]Safran Tech, Châteaufort, 78114, Magny-les-Hameaux, France[†].
[3]UCLouvain, Louvain-la-Neuve, 1348, Belgium.
[4]ULiège, Liège, 4000, Belgium.

*Corresponding author(s). E-mail(s): margaux.boxho@cenaero.be;
Contributing authors: gregory.dergham@safrangroup.com;
gregoire.winckelmans@uclouvain.be; koen.hillewaert@uliege.be;

**Abstract**

Wall models reduce the computational cost of large eddy simulations (LES) by modeling the near-wall energetic scales and enable the application of LES to complex flow configurations of engineering interest. However, most wall models assume that the boundary layer is fully turbulent, at equilibrium, and attached. Such models have also been successfully applied to turbulent boundary layers under moderated adverse pressure gradients. When the adverse pressure gradient becomes too strong, and the boundary layer separates, equilibrium wall models are no longer applicable. In this work, the relations between the instantaneous wall shear stress, velocity field, and pressure gradients are evaluated using space-time correlations for the purpose of analyzing the near-wall physics in different flow configurations. These correlations are extracted from two wall-resolved LES: a channel flow at a friction Reynolds number $\mathrm{Re}_\tau$ of 950 and the two-dimensional periodic hill at a bulk Reynolds number $\mathrm{Re}_b$ of 10595. This analysis highlights that no instantaneous and local correlation is observed in the vicinity of the separation. The domain of high correlation appears to be shifted downstream. This study of the near-wall physics is a step for developing a data-driven wall model applied to separated flows and, in particular, selecting suitable input parameters for the training of neural networks.

[†]Digital Sciences & Technologies Department, Rue des Jeunes Bois.

**Keywords:** Space-time correlations, ILES, Separated flows, Near-wall physics, Wall-models

# 1 Introduction

In off-design conditions, the flow inside turbomachinery components is dominated by complex features, which are outside the range of reliability of RANS turbulence models. It is, therefore, desirable to perform high-resolution simulations with much fewer modeling assumptions. LES is a valuable tool for the numerical prediction of the physics of transitional and turbulent flows in more realistic configurations than Direct Numerical Simulations (DNS). Nonetheless, wall-resolved LES (wrLES) methods, where the wall-nearest grid point is within the viscous sublayer, remain prohibitively expensive at high Reynolds numbers typical of most turbomachinery passages. In wall-modeled LES (wmLES), the wall-nearest region is coarsened to reduce the computational cost, which moves the first grid point away from the viscous sublayer. The effect of the unresolved near-wall physics is then usually represented by a shear stress boundary condition computed from a wall model that depends on flow quantities inside the computational domain.

The first attempt to apply a wall model was made by Deardoff [15], who simulated a channel at an infinite Reynolds number. A few years later, Schumann [40], while working on channel flows at finite Reynolds numbers, defined conditions that directly link the velocity in the core to the wall shear stress components. In his approximated boundary condition, the mean stress was set equal to the given pressure gradient. Grötzbach [23] rather considered the logarithmic law from which the mean stress was computed iteratively. He extended Schumann's boundary condition to flow configurations where the pressure gradient was not known *a priori*. By requiring the wall shear stress to be correlated to the instantaneous velocity, Piomelli *et al.* [34] introduced a downstream displacement $\Delta_s$ to their model, called the shifted boundary conditions. This enhancement was based on the inclination of elongated structures near the wall studied by Rajagopalan and Antonia [37]. Piomelli *et al.* [34] also proposed the ejection model based on the observation that the high-velocity fluid motion towards or away from the wall occurring during sweep-eject events significantly affects the wall stress.

To overcome the assumption that the logarithmic law-of-the-wall holds in the mean, Mason and Callen [31] extensively worked on the enforcement of the logarithmic law locally and instantaneously while imposing the alignment of the wall shear stress with the outer horizontal velocity. They reported that the validity of this assumption depended on the size of the averaging volume. Werner and Wengle [47] used a power law to compute the local stress. The work of Hoffmann and Benocci [24] and Wang [46] was based on the integration of the boundary layer equations coupled with an algebraic turbulent

model. Nicoud *et al.* [33] pointed out that most models performed poorly at high-Reynolds numbers, even in channel flows. They overcame this issue by applying a suboptimal control theory to force the outer LES towards a desired mean velocity profile. Although this method was expensive, it generated tables of correlations between the outer velocity and wall stress that accounted for numerical and SGS errors. They finally derived from linear stochastic estimation (LSE) a wall model that gave encouraging results up to $Re_\tau$ 20,000. Abel *et al.* [1] generalized Schumann's model, Piomelli *et al.*'s model, the ejection model, and the gradient model by using generalized additive models (GAM) and nonlinear, nonparametric regression. The authors analyzed the near-wall physics and discovered a strong influence of the pressure gradient in the viscous sublayer.

For complex, unsteady, and non-equilibrium flow features, including secondary flows and massive separation, most of the above methods fail because they rely on the laws of the wall valid for attached flows at moderate pressure gradients. These models do not account for pressure gradients and other effects relevant to separation. The Two-Layer Model (TLM) initially proposed by Balaras *et al.* [2] was a first zonal approach developed to tackle more complex flows. Although the TLM was applied to the numerical simulation of square ducts, rotating channels, and backward-facing steps, to name but a few, the method still suffers from two problems: the log-layer mismatch and the resolved Reynolds stresses inflow. Another zonal approach is the Detached Eddy Simulation (DES) which applies RANS calculations in attached boundary layer regions and LES calculations in separated flows. Such a method was initially proposed by Spalart *et al.* [39]. The concept of artificial viscosity was also used in the work of Breuer *et al.* [6]. They claimed that a simple model of the artificial viscosity can be used if an appropriate definition of the relative thickness of the viscous sublayer is obtained. They compared their analytical model with different variations of Werner-Wengle's model on the two-dimensional periodic hill at $Re_b = 10595$ and got encouraging results. More recently, Cadieux *et al.* [8] addressed the separation problem using an integral wall model for LES with additional non-equilibrium terms. They managed to obtain an analytically tractable integral formulation and successfully applied it to a flat plate subjected to an adverse pressure gradient. The work of Krank *et al.* [28] consists of the enrichment of the Discontinuous Galerkin (DG) solution using a turbulent boundary layer velocity profile model. This approach was successfully applied to channel and periodic hill flows. Although much progress has been achieved in this field, most existing equilibrium wall models [4, 36] are still not able to predict flow separations and reattachments.

The current research aims at exploiting the approximation capabilities of deep neural networks (DNNs), described first by Hornik [25], to establish a more general model for the complex relationship between instantaneous flow fields, geometrical parameters, and wall shear stress using DNS or wrLES databases. More recently, the scientific community has used Machine Learning (ML) and Deep Learning (DL) techniques to address various challenges in fluid

dynamics, flow control, and optimization with (experimental and/or numerical) data [7, 16]. A first application of DNN to wall modeling is presented in the work of [48], which incorporates *a priori* physical knowledge into the model input to enhance the extrapolation capabilities at higher Reynolds numbers. Zhou *et al.* [49] target the turbulence separation by working on the periodic hill. Although they obtained satisfactory *a priori* results, the *a posteriori* validation completely fails in predicting the mean velocity profile on the nominal geometry at Re = 10595. Lozano-Duran [29] hypothesized that any complex flow can be decomposed as a non-linear combination of simpler flows, called *building-block flows*. In their work, a wall-flux-based wall model for LES using a self-critical machine-learning approach was successfully trained on DNS data (e.g., flow over a flat plate, in a channel, in a turbulent duct, or separated flow at various Reynolds numbers). However, the application of the model to the NASA Juncture Flow fails to correctly predict the separation. This failure is attributed to a lack of training data.

For the development of wall models for separated flows using deep neural networks, the future model should have the following specifications: (a) local, (b) small (i.e., a small number of parameters for fast inference), and (c) generalizable. The former is crucial to generate a model that depends neither on geometry nor on global quantities. To enforce (b), feature selection is applied to reduce the problem dimensionality and remove irrelevant and redundant features from the dataset. As Piomelli *et al.* [34] argued, a wall shear stress correlated with the instantaneous velocity is desirable. This statement is even more relevant when training deep neural networks for which the input/output labels should be highly correlated. To ensure the dimensionality reduction and to find highly correlated input/output labels, a space-time correlation analysis between the instantaneous wall shear stress $\boldsymbol{\tau}_w$ and flow variables (e.g., $\mathbf{v}$ and $\nabla p$) measured in the nearby volume is performed. This paper is therefore dedicated to the investigation of the near-wall physics of different flow configurations. One of the first attempts to detect properties of large structures in fully developed turbulence is the work of Rajagopalan and Antonia [37] in which they analyzed space-time correlations between the wall shear stress and the velocity fluctuations. They examined the wall-normal evolution of the correlations and observed the inclination of large structures that had inspired Piomelli *et al.* [34] for their shifted approximated boundary condition. A few years later, Colella *et al.* [13] performed similar measurements in a channel flow and conclude that the angle of inclination of the large convected structures depends on the Reynolds number. It is known that the modeling of wall turbulence is still a major concern. The Attached Eddy Model of Townsend [43–45] has proven to be highly effective in the prediction of velocity statistics. It also provides a framework for interpreting the energy-containing scales at high Reynolds numbers [30]. In the analysis of near-wall physics, the focus is on turbulence in the presence of a wall. The wall imposes an inhomogeneous direction responsible for additional complexities such as scale separations, and

significant anisotropy, to name a few. The work of McKoen [32] reviews certain aspects of the interpretation and treatment of mechanisms of turbulence maintenance in wall turbulence for parallel flows with canonical boundary conditions. Dawson and McKoen [14] focused on the identification of pertinent structures in turbulent wall-bounded flows. The method was explicitly tested on a turbulent boundary layer and both laminar and turbulent channel flows. The work of Cheng *et al.* [12] is also dedicated to the analysis of near-wall physics by detecting high and low-speed structures of the streamwise wall-shear fluctuations using a two-dimensional clustering methodology. These structures were classified into positive and negative families (PFs and NFs) motivated by the presence of nonlinear interactions and energy transfer between inner and outer scales. Indeed their work emphasizes several asymmetries between PFs and NFs. They conclude that NFs are actively connected to the attached eddies that populate the logarithmic region.

The analysis of near-wall physics done in the works cited above is mainly performed for equilibrium flows such as flat plate and turbulent channel flows. In our approach, we target equilibrium and non-equilibrium conditions with two test cases: (i) a turbulent channel flow at a friction Reynolds number ($Re_\tau$) of 950 and (ii) the well-known two-dimensional periodic hill, at bulk Reynolds number ($Re_b$) of 10595. Out of these two test cases, three distinct configurations of increasing complexity are defined: (i) the solid wall of the channel, (ii) the upper wall of the periodic hill, and (iii) the lower wall of the periodic hill. The channel flow is a common geometry for which the wall models have been successfully applied. Concerning (ii), the flow is also turbulent, attached, and at equilibrium. However, it is subjected to a moderate pressure gradient that modifies the mean wall shear stress. Finally, the third configuration presents a massive separation on a curved geometry. Using these three configurations, the impact of these complexities (i.e., curved wall, moderate pressure gradient, and separation) is carefully analyzed using space-time correlations. Based on these test cases, space-time correlations between the velocity, pressure gradients, and the wall shear stress in the wall-normal direction but also in the streamwise and spanwise directions are evaluated.

The remainder of this paper is structured as follows. In Section 2, the methods adopted in this work are described. The space-time correlations are presented in Section 3 and 4 for the channel and periodic hill test case, respectively. Conclusions are finally drawn in Section 5.

## 2 Method

The two types of correlations considered in this work to perform feature selection are presented in Section 2.1. The numerical method used to perform a wrLES of the channel and the two-dimensional periodic hill is also briefly explained in Section 2.2.

## 2.1 Space-time correlations

Although turbulent flows appear highly disorganized and are unpredictable in their exact behavior, they are described by deterministic equations and often have statistically stationary solutions. Consequently, any turbulent flow quantity can be decomposed into means and fluctuations in space and time. To further characterize the flow behavior and define the input of our data-driven wall model, relations between the velocity, the pressure gradient, and the wall shear stress are sought in space and time. The correlations are first measured on a well-known geometry: the turbulent channel flow. The analysis is then extended to a more complex configuration: the two-dimensional periodic hill. The latter is subdivided into an upper and lower solid wall. The upper wall is exposed to the pressure gradient generated by the free shear layer, while the lower wall is subjected to separation and reattachment.

As a first step, the correlation coefficient is computed. This coefficient is a single number that condensates the strength of dependence. The most popular correlation coefficient is the classical Pearson correlation (see [17]). It measures the strength of linear dependencies between random variables. Although the independence between two random variables implies a zero correlation, the reverse implication is false. Alternative correlation coefficients have been proposed to avoid this drawback. Among those alternatives, the distance correlation coefficient, proposed by Székely et al. [41], is considered.

**The Pearson correlation** can be extended to handle time delay $\delta t$ and space shift $\delta\xi$ (see Figure 9) as follows,

$$R(\delta t, \delta\xi) = \frac{\langle u(\mathbf{x} + (\delta\xi)\hat{e}_\xi, t_0 + \delta t)\tau_w(\mathbf{x}, t_0)\rangle}{\sqrt{\langle u^2(\mathbf{x}, t_0)\rangle}\sqrt{\langle \tau_w^2(\mathbf{x}, t_0)\rangle}}, \tag{1}$$

where $\boldsymbol{x}$ is $(\xi, \eta, z)$ (as defined in Figure 9) and $\hat{\xi}$ is the unit vector in the $\xi$-direction. $u$ and $\tau_w$ are the fluctuations of tangential velocity and wall shear stress taken in the wall parallel direction, respectively. The operator $\langle\cdot\rangle$ stands for time and spanwise average. Note that the forcing term is extracted from the pressure gradients. From now, the velocity (or pressure gradients) will refer to the spatial variations of the temporal fluctuations of the velocity (or the spatial variations of the temporal fluctuations of pressure gradient).

**Distance correlation.** A similar exercise is performed for the sample distance correlation to account for space shift and time delay. Assuming that $X = u(\mathbf{x}+\delta\xi, t_0+\delta t)$, $Y = \tau_w(\mathbf{x}, t_0)$ and two realizations of size $n$, the sample distance covariance measured at $(\delta\xi, \delta t)$ is defined as

$$\mathrm{dCor}(X, Y) = \frac{\mathrm{dCov}(X, Y)}{\sqrt{\mathrm{dVar}^2(X)\,\mathrm{dVar}^2(Y)}}, \tag{2}$$

where $\mathrm{dCov}(X,Y)$ is the distance covariance between $X$ and $Y$ computed as

$$D_n^2(X,Y) = \frac{1}{n^2}\sum_{j=1}^{n}\sum_{k=1}^{n} A_{j,k}B_{j,k}\ . \tag{3}$$

In this last expression, $A_{j,k}$ and $B_{j,k}$ are two matrices of size $n \times n$ where $A_{j,k}$ is computed as $A_{j,k} := a_{j,k} - \overline{a}_{j.} - \overline{a}_{.k} + \overline{a}_{..}$ where $\overline{a}_{j.}$ is the $j^{th}$ row mean, $\overline{a}_{.k}$ is the $k^{th}$ column mean and $\overline{a}_{..}$ is the grand mean of the distance matrix. The distance matrix of $X$ is defined as $a_{j,k} = \|X_j - X_k\|, \quad j,k = 1,2,\cdots,n$ where $\|.\|$ denotes the Euclidean norm. The same applies to $Y$ to form the matrices $b_{j,k}$ and $B_{j,k}$. Finally, the sample distance variance is defined as: $\mathrm{dVar}^2(X) := D_n^2(X,X) = \frac{1}{n^2}\sum_{k,l} A_{k,l}^2$. The brute force algorithm to compute the distance correlation is $\mathcal{O}(n^2)$. The $\mathcal{O}\left(n\log(n)\right)$ algorithm, proposed in [11], has been implemented.

## 2.2 Simulations details

Two different test cases the turbulent channel flow (Section 3.1) and the two-dimensional periodic hill (Section 4.1) are simulated with the code Argo-DG, which is a high-order Discontinuous Galerkin (DG) flow solver, developed at Cenaero, that solves the compressible Navier-Stokes equations. This solver, developed during the thesis of K. Hillewaert [27], implements the Discontinuous Galerkin method, with the symmetric interior penalty method (SIP). The code can handle large cases thanks to the high scalability of the DG method. It uses a hybrid parallelism based on *message passing interface* (MPI), and *open multi-processing* (OpenMP). DG methods (DGM) are a particular class of the Galerkin finite element method (FEM) where the shape functions (e.g., Lagrange polynomials of order $p$) defined in each element are not required to be continuous across the interfaces. This feature leads to a compact and local set of discretized equations on the element. Although this discretization is the key to the high scalability of the overall method, it needs to be stabilized with consistent penalty terms on the element interfaces. For this purpose, a Riemann solver is used for the convective terms, while diffusive terms are controlled by the SIP method. Regarding time discretization, an implicit method is selected because it allows a larger time step than the time-explicit method for which the time step is drastically constrained by the CFL condition. At each time step, a non-linear problem resulting from the implicit integration is solved through a Newton/GMRES method, preconditioned with elementwise block-Jacobi.

In terms of turbulence modeling, Argo-DG relies on the implicit LES (ILES) approach, for which the numerical dissipation of the underlying high-order DG scheme spectrally acts similarly to the explicit sub-grid scale models traditionally used in classical LES methods [10].

## 2.3 Parameters

The Pearson and distance correlations presented above are computed for a channel flow at $Re_\tau = 950$ and the two solid walls of a periodic hill at $Re_b = 10,595$ in Section 4. The objective is to detect high correlations between the wall shear stress and volume fields (e.g., velocity, pressure gradients). Correlations in the streamwise (or spanwise periodic) wall-parallel direction generate two important parameters for the development of a data-driven wall model: a time delay $\delta t$ and a space shift $\delta\xi$ (or $\delta z$, respectively). These parameters are scaled differently for the channel flow and the periodic hill.

- For the channel flow (Section 3), the scaling is the known wall unit normalization, assimilated to the subscript $+$, using the viscosity $\nu$ and the friction velocity $u_\tau$ defined as $u_\tau = \sqrt{\tau_w/\rho}$, where $\tau_w$ is the mean wall shear stress and $\rho$ is the density.
- For the periodic hill (Section 4), the scaling uses a length scale $h$ (i.e., the hill height) and a velocity scale $u_b$ (i.e., the bulk velocity).

Table 1 lists all the possible correlations. Among all these correlations, only significant correlations are examined in this work.

**Table 1**: List of all combinations of correlations between velocity (or pressure gradients) and wall shear stress.

| *Wall shear stress* | *Velocity* | | | *Pressure gradients* | | |
|---|---|---|---|---|---|---|
| | $u_\xi$ | $u_\eta$ | $u_z$ | $\frac{\partial p}{\partial \xi}$ | $\frac{\partial p}{\partial \eta}$ | $\frac{\partial p}{\partial z}$ |
| $\tau_{w,\xi}$ | $U0T0$ | $U1T0$ | $U2T0$ | $P0T0$ | $P1T0$ | $P2T0$ |
| $\tau_{w,z}$ | $U0T2$ | $U1T2$ | $U2T2$ | $P0T2$ | $P1T2$ | $P2T2$ |

To make a fair comparison between the channel flow and the periodic hill, correlations map in space ($\delta\xi$) and time ($\delta t$) are computed. Unless otherwise stated, contours at 85% are drawn as thin black lines to highlight a domain of high correlation, noted $\mathcal{D}$. In the presence of anti-correlations, white dashed lines are drawn instead. These contours are defined as:

$$\mathcal{C}(f(\delta t, \delta\xi)) = \alpha \max\left(|f(\delta t, \delta\xi)|\right) , \tag{4}$$

where $\alpha = 0.85$ and,

$$f(\delta t, \delta\xi) = \begin{cases} R(\delta t, \delta\xi) & \text{for Pearson correlation.} \\ D(\delta t, \delta\xi) & \text{for Distance correlation.} \end{cases}$$

Sections 3 and 4 are organized as follows. Firstly, the flow statistics are well described and fairly compared with available literature. Secondly, Pearson and distance correlations are presented and analyzed for relevant combinations between the velocity field (or pressure gradients) and the wall shear stress.

Three types of space-time correlations are evaluated: (i) the space corresponds to a displacement $\delta\xi$ in the streamwise wall-parallel direction $\xi$, (ii) the space corresponds to a displacement $\delta z$ in the spanwise wall-parallel direction $z$ and (iii) the space corresponds to a given distance from the wall in the wall-normal direction. These correlations are used to select inputs to implement a data-driven wall model and better understand the flow physics near separation.

# 3 Channel at $Re_\tau = 950$

It is well-known that existing wall models work well on channel flow because it is fully turbulent, attached, and at equilibrium. In these wall models [23, 40], the prediction of the wall shear stress is performed with the velocity taken above the point where $\boldsymbol{\tau}_w$ is required, except in the work of Piomelli *et al.* [34] where the velocity is taken downstream along a given structure. Therefore, as a preliminary consideration, it is expected that the correlations will show a slight space-time lag which may depend on the height at which the correlation is assessed.

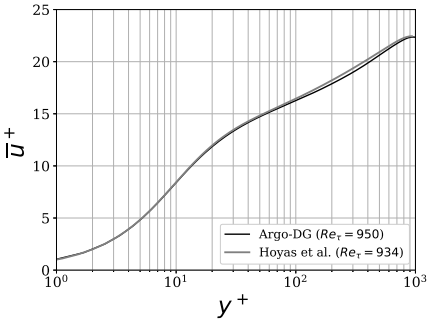


(a) Mean velocity profile $u^+$ in wall units

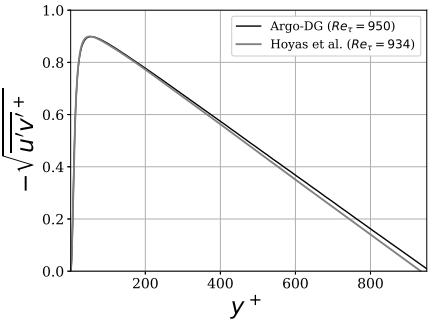


(b) Covariance of $u$ and $v$ in wall units

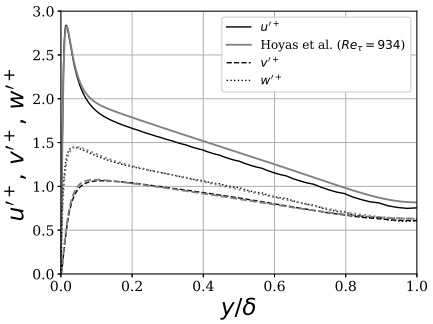


(c) RMS velocity profiles in global coord

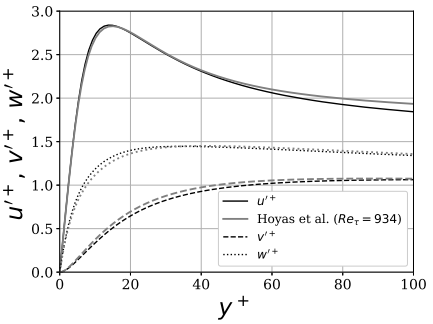


(d) Velocity RMS profiles in wall units

**Fig. 1**: Standard flow statistics of the channel flow at $Re_\tau = 950$, compared to the results of Hoyas et al. [26]

## 3.1 Flow statistics

The geometry of the channel flow test case is periodic and homogeneous in the streamwise and spanwise directions. The flow is enclosed between two solid walls separated by a distance $2\delta$ [26]. The computational domain sizes are $L_x/\delta = 2\pi$ and $L_z/\delta = \pi$. The flow is driven by a uniform pressure gradient. The Mach number is set to a low value ($M = 0.1$) for a fair comparison with the incompressible flow references. The simulation is performed with a mesh resolution comparable to a wrLES: $\Delta x^+ \simeq 90$ and $\Delta z^+ \simeq 46$, where the superscript $+$ denotes the wall unit normalization. The Lagrange polynomial order $p$ is set to 3 which gives an effective resolution of $\Delta x^+ \simeq 30$ and $\Delta z^+ \simeq 15$. Close to the wall, the effective resolution is set such that $\Delta y^+ \simeq 1$. After evacuating the numerical transient, the statistics have been accumulated for approximately $13,870\, t^+$, where $t^+$ is defined as $t\, u_\tau^2/\nu$. It corresponds to 45.8 flow-through time ($t_c$), defined as $t\, u_b/L_x$, where $u_b$ is the bulk velocity. The implicit integration scheme is there to overcome the restrictive acoustics-induced CFL condition in the near-wall region, where a $y^+ = 1$ is asked to perform a good wall-resolved LES. However, the convective CFL number was kept at about 0.3 to ensure that turbulence-related time structures are properly resolved by the time discretization. Figure 1 shows the standard statistical data on the channel. The mean velocity profile in wall units is almost perfectly superimposed on the reference [26] (in gray). One can also notice a good agreement of $u^+$ in the near-wall region (Figure 1a). Examining the covariance between $u$ and $v$ (Figure 1b), the straight line, typical of wall-bounded flows, is recovered. The two curves slightly go apart as $y^+$ increases due to a small difference in $Re_\tau$. The profile obtained with Argo-DG (in black) crosses the horizontal axis at $y^+ \simeq 957.0$. Regarding the rms velocity profiles, a fair agreement with reference [26] is obtained in the near-wall region (Figure 1d) while at the center of the channel, the fluctuations $u'^+$ are lower than the reference data. The two other RMS profiles are, on their own, well predicted at the channel center (Figure 1c).

## 3.2 Pearson and distance correlations in the streamwise direction

All correlations for the channel are calculated at a wall-normal distance of $y^+ \simeq 100$, which is still close enough to the wall to feel its interaction but large enough to be in the logarithmic layer. Note that the streamwise direction is homogeneous, which allows the averaging of multiple realizations of the correlations in such a direction to accelerate the convergence of the statistics. For a channel flow, the most significant correlations are $U0T0$ and $U1T0$ (as defined in Table 1). Moreover, no correlation has been found between the velocity field and the spanwise wall-shear stress. Besides, no relation has been found between the pressure gradients and the wall shear stress at the considered wall-normal distance. This observation is coherent with the work of Abel *et al.* [1] who only found a correlation between the pressure gradient and the wall shear stress in

the viscous sublayer. This correlation quickly decreases with the increase of the wall distance. Hence, it is the velocity field that triggers the wall shear stress.

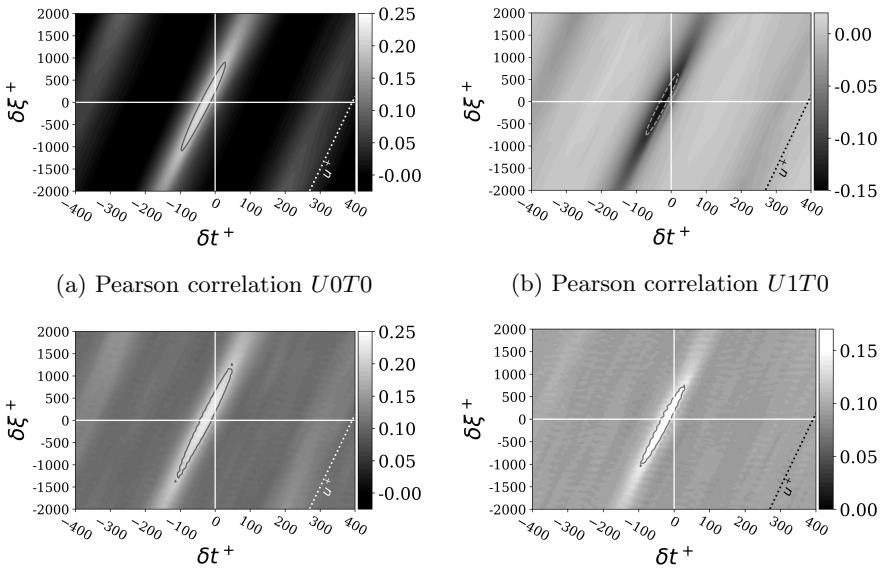


(a) Pearson correlation $U0T0$

(b) Pearson correlation $U1T0$

(c) Distance correlation $U0T0$

(d) Distance correlation $U1T0$

**Fig. 2**: Space-time correlations in the streamwise direction evaluated on the channel at $Re_\tau = 950$ at a wall-normal distance of $y^+ = 100$, the local averaged streamwise velocity $u^+$ is drawn in dotted line

### *Correlation* $U0T0$

The correlation $U0T0$ for a zero displacement is shifted over $-30\delta t^+$ in time. It corresponds to a normalized downstream displacement of approximately 450 which is coherent with experimental results that gives $\delta\xi^+ = |y^+|cot(13°) \simeq 433$ for large distance from the wall [35]. It aligns with the mean streamwise velocity $u^+$, which corresponds to the local convection velocity (see Figure 2a). The distance correlation, displayed in Figure 2c, reveals a similar domain of high correlation $\mathcal{D}$. Its amplitude indicates a non-linear relation between $u_\xi$ and $\tau_{w,\xi}$. We can conclude that: if local information is used, a time delay needs to be accounted for $u_\xi$. Similarly, if instantaneous information is only used, a space shift needs to be considered due to the streamwise convection of the near-wall structures.

### *Correlation* $U1T0$

In Figure 2b, the relation between $\tau_{w,\xi}$ and $u_\eta$ is anti-correlated: When the wall-normal velocity increases, the wall shear stress will tend to decrease, and

thus the friction is reduced. This observation is coherent with flow ejections that tend to decrease the wall shear stress as explained in [34] in their ejection model. The distance correlation, exposed in Figure 2d, indicates a similar $\mathcal{D}$ as the Pearson correlation but with a positive value of 16% because this correlation is based on a measurement of a distance in the $L_1$-norm (Equation 2) and therefore can only take a positive value. $\mathcal{D}$ is shifted the same way as $U0T0$, and similar wall models' best practices are drawn.

***Wall-normal evolution of*** $U0T0$

Figure 3a shows the wall-normal evolution of $U0T0$ without any streamwise displacement (i.e., $\delta\xi = 0$). The two variables are highly correlated at $\delta t^+ = 0$ close to the wall (at the beginning of the buffer layer). With increasing distance from the wall, the correlation between the fluctuations decreases, and the correlation peak is shifted in $\delta t < 0$. According to Colella et Keith [13], this increase in time delay as moving away from the wall implies the existence of an angle of inclination of structures convected along the wall. The decrease in amplitude is due to the decay in these convected structures.

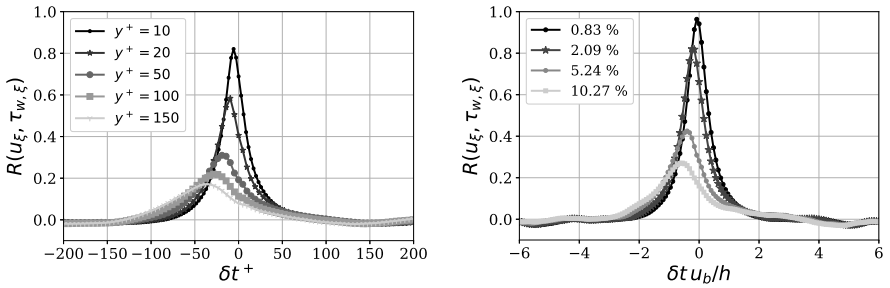


(a) For the channel at $Re_\tau = 950$, average over every streamwise positions

(b) For the periodic hill at $Re_b = 10,595$ at $x/h \simeq 9.0$ on the upper solid wall

**Fig. 3**: Evolution of the time correlation (for $\delta\xi = 0$) as going away from the solid wall (a) in wall units and (b) in % of the hill height $h$

### 3.2.1 Pearson correlations in the spanwise direction

As for the streamwise correlations, $U0T0$ and $U1T0$ are the only significant correlations observed. Cross correlations as $U2T0$, $U0T2$, and $U1T2$ are not visible at $y^+ = 100$ but appear at lower $y^+$ values (not shown here). They are symmetric around $\delta z = 0$ with two lobes (one positive and one negative) of similar amplitude as those observed for the periodic hill in Section 4 (see the right-most graph in Figure 20).

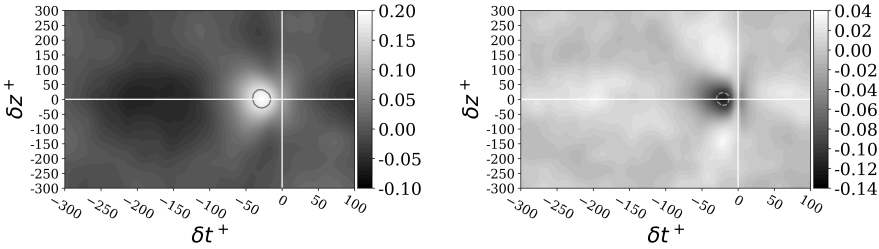


(a) Pearson correlation $U0T0$ (b) Pearson correlation $U1T0$

**Fig. 4**: Space-time correlations in the spanwise direction evaluation on the channel at $Re_\tau = 950$ for a wall-normal distance of $y^+ = 100$

***Correlations*** $U0T0$ ***and*** $U1T0$

Since there is neither a skewed boundary layer nor a spanwise pressure gradient in a channel flow, the spanwise wall shear stress $\tau_{w,z}$ is zero on average. Due to this observation, the domain of high correlation $\mathcal{D}$ in the spanwise direction is narrow and symmetric. Indeed, the correlation map of $U0T0$ (see Figure 4a) is spread over only about twenty wall units and is symmetric with respect to $\delta_z^+ = 0$. The domain of high correlation $\mathcal{D}$ is aligned with $\delta z/h = 0$ due to the absence of convection along this direction. Nonetheless, the correlation peak is shifted in $\delta t^+ < 0$ for $y^+ = 100$. For $U1T0$ (see Figure 4b), this time delay and the spreading along the z-direction are similar. As for the streamwise correlation $U1T0$, Pearson correlation also measures an anti-correlation.

### 3.2.2 Correlations on the channel: conclusion

As a final remark, the wall shear stress is strongly dependent on the streamwise velocity while the wall-normal velocity has a reverse impact on $\tau_{w,\xi}$ as explained by ejection effects. All correlations, in both streamwise and spanwise directions, show a time delay when moving away from the wall: The correlation peak is shifted in $\delta t^+ < 0$. The mean velocity that convects structures across the domain increases with distance from the wall. This phenomenon promotes the inclination of structures as explained by Colella and Keith [13] and earlier by Rajagopalan and Antonia [37]. To compensate for this convection, and thus the spatial displacement of the structures along the wall, a time delay is identified in the correlations. Otherwise, if no time delay is considered, a space displacement is pinpointed. Both $\delta t$ and $\delta\xi$ are related to the local mean velocity, as shown in Figure 5. According to this observation, the wall model can remain local if a short time delay is considered. This procedure holds if the numerical time step of the wall model $\delta t_{wmLES}$ is visible in regards to the delay measured in these correlations. Otherwise, a downstream shift can be considered as in the shifted boundary condition model of Piomelli *et al.* [34].

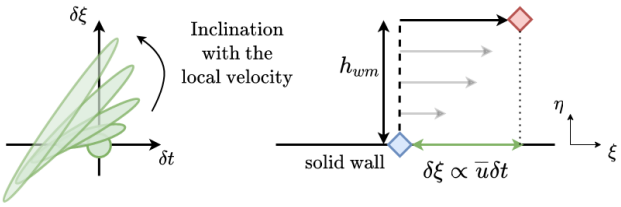


**Fig. 5**: Explanation of the inclination of the correlations and the time delay experienced when moving away from the wall

# 4 Two-dimensional periodic hill at $Re_b = 10,595$

This section is organized the same way as Section 3. Nonetheless, the analysis of the periodic hill is divided between the upper wall (Section 4.2) having a behavior similar to that of a channel wall, except that it is subjected to a moderate pressure gradient, and the lower wall (Section 4.3) characterized by a massive separation followed by a reattachment on the flat bottom part of the wall.

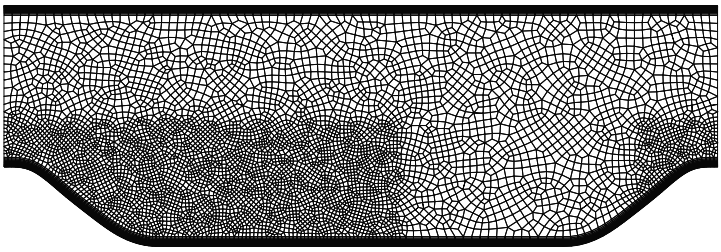

(a) Unstructured 3D-extruded mesh, used for the simulation of the two-dimensional periodic hill at $Re_b = 10,595$

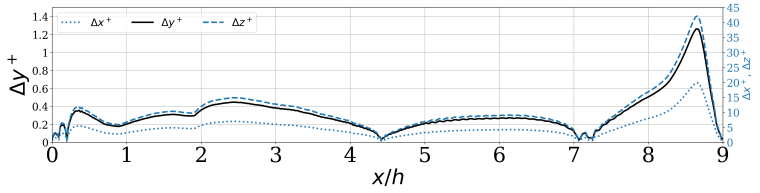


(b) Averaged grid refinements $(\Delta x^+, \Delta y^+, \Delta z^+)$ in wall units computed from the averaged wall shear stress

**Fig. 6**: Mesh information

## 4.1 Flow statistics

This flow consists of a bi-periodic flow between two walls with a streamwise constriction. It combines carefully chosen characteristics resulting in flow separation, recirculation, and reattachment. The first hill is located at $x/h = 0$ and the second at $x/h = 9$. The streamwise periodicity is hence fixed to $L_x/h = 9$. The spanwise periodicity is fixed to $L_z/h = 4.50$. The flow is driven by a constant pressure gradient whose magnitude is controlled to match the bulk Reynolds number, defined as $Re_b = \frac{u_b h}{\nu}$, using the procedure proposed by Benocci and Pinelli [3], where small modifications have been introduced by Carton de Wiart [9] to account for compressibility. This test case is part of the ERCOFTAC KB Wiki, and has been extensively studied both numerically, e.g. see [5, 22], and experimentally by Song and Eaton [38]. We refer to Fröhlich *et al.* [21] for the description of the 3D extruded geometry and a detailed discussion of the flow behavior. The flow has been simulated for a bulk Mach number $M_b = 0.1$, and statistical data have been accumulated over more than 38 flow-through times, after evacuating the numerical transient during 45 flow-through times. The mesh (Figure 6a) is composed of 445,005 hexahedra. In the near-wall regions (up and down walls, where a no-slip wall boundary condition is imposed), representing 10% of the hill height, the mesh is structured with a geometry progression to impose a size of the first cell at the wall corresponding to $y^+ = 1$ (see Figure 6b). The averaged grid refinements in the streamwise and spanwise direction, in wall units, are 5 and 10, respectively. The rest of the mesh is unstructured with a refinement region located near the separation and in the free shear layer. The simulation is performed with Lagrangian interpolants of order $p = 3$, to give a total of 28,480,320 degrees of freedom. Considering the bulk velocity $u_b$, the spatial resolution of the mesh near the separation, the polynomial order of the DG method, and the imposed time step, the convective CFL is also maintained at about 0.3, which ensures that turbulence-related time structures are properly resolved for computing the space-time correlations.

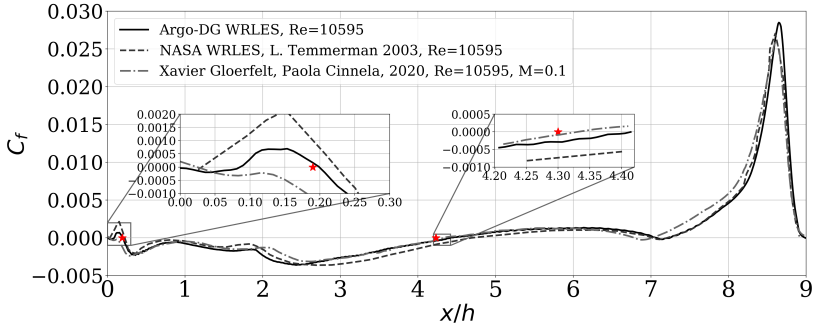


**Fig. 7**: Friction coefficient $C_f$ measured on the bottom surface of the periodic hill at $Re_b = 10,595$, compared to [22, 42]

The averaged results are compared to [5, 22]. Examining the mean velocity profiles and the Reynolds stresses, a good agreement with respect to the references is observed (see Figure 8). Figure 7 depicts the friction coefficient defined as $u_\tau^2/(0.5\rho u_b^2)$. A good match is noted with the results obtained by [22] at $M = 0.1$. A precursory separation is visible at $x/h \simeq 0$, explained by a high-pressure gradient region that emerges downstream of a low-pressure area located at $x/h \simeq 8.75$. This tiny separation is hence visible at the hilltop due to these high-pressure gradients. Such region produces eddies of high kinetic energy that are convected downstream and affect the separation process on the curve wall [6]. The main separation appears at $x/h \simeq 0.2$. Around $x/h \simeq 2.0$, the flow decelerates and then re-accelerates due to the change in curvature. We notice that the deceleration/acceleration process is slightly shifted for the dash-dotted $C_f$ curve in Figure 7. At the windward base of the hill, [22] predicts a small separation before $x/h = 7.0$. These two discrepancies with [22] are probably due to the geometric definition of the lower wall and, more precisely, the connection between the bottom flat part and the hill. The reattachment location is well captured. The recovery region goes from $x/h \simeq 4.2$ to $x/h \simeq 7.0$, with a secondary recirculation bubble at $x/h \simeq 7.2$, followed by a strong acceleration while ascending.

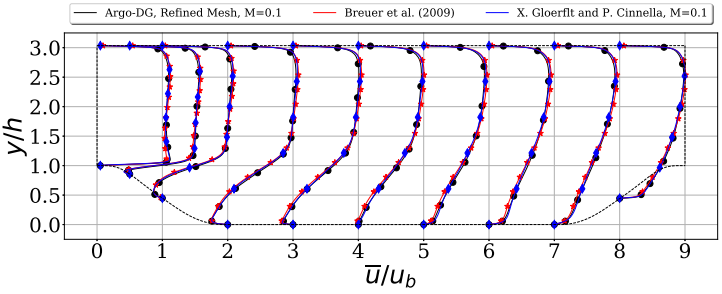


(a) Averaged velocity

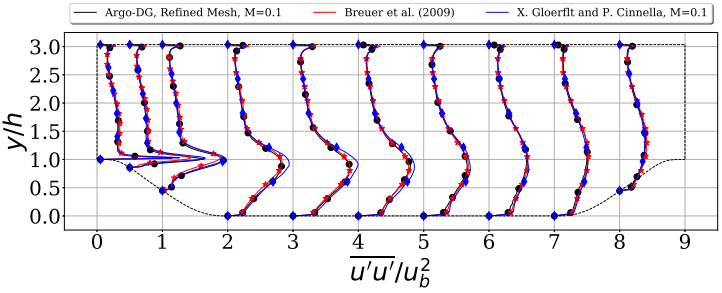


(b) Reynolds stress component

**Fig. 8**: Flow statistics of the periodic hill at $Re_b = 10,595$, compared to [5, 22]

## 4.2 Analysis of space-time correlations on the top wall of the periodic hill

The upper wall of the periodic hill geometry is comparable to a channel wall, in that respect that it does not feature any curvature. However, the streamwise direction is not homogeneous due to the strong fluctuations of the pressure gradient generated by the complex dynamics occurring on the lower solid wall (i.e., separation, reattachment, unsteady free shear layer, recirculation bubble, turbulence recycling due to the periodicity assumption).

The correlations are illustrated for three distinct regions: the separation $S$, the reattachment $R$, and the converging region $C$ (see blue diamonds in Figure 9). All correlations are computed at a given wall-normal distance of 10% of the hill height $h$, for both the upper and lower wall. In terms of $y^+$, this height corresponds to a value between 20 and 40 for $x/h \in [0, 8]$ and 100 along the converging part, for the lower wall. For the upper wall, such a wall-normal height corresponds to values between 50 to 70. Instead of using the Cartesian coordinates to describe this geometry, the curvilinear coordinates are selected. This coordinate system, for the lower wall, is defined in Figure 9. Each field is projected on the local frame of reference defined by the geometry.

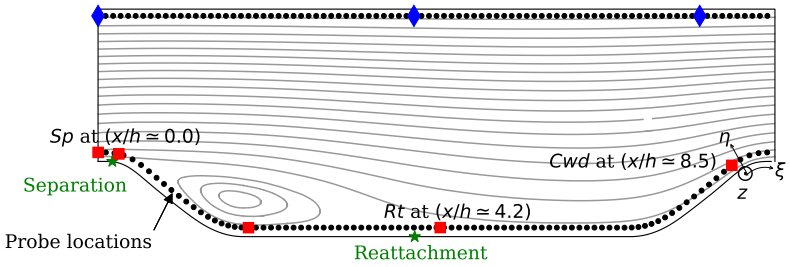


**Fig. 9**: Probe positions at a given wall-normal height ($\eta/h \simeq 0.1$) (upper and lower wall) and location of the observation points along the lower wall (red square) and the upper wall (blue diamond)

### 4.2.1 Streamwise Pearson and distance correlations

Among all streamwise correlations between the velocity field and $\tau_w$, only $U0T0$, $U1T0$, and $U2T2$ are discussed, whereas for the pressure gradients, only the "aligned" correlations $P0T0$ and $P2T2$. Since these correlations are similar in shape and amplitude for the three selected positions, they are presented for the separation location only. However, the amplitude is different at reattachment, with a decrease in magnitude of 10 to 20%.

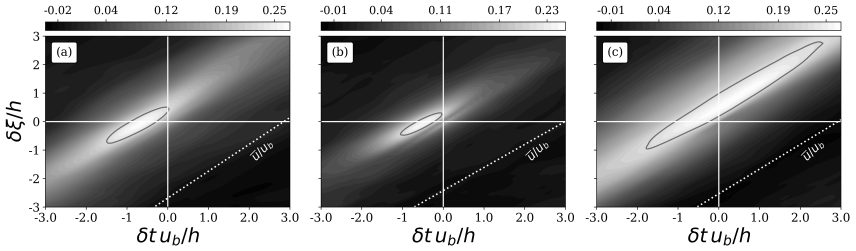


(a) Pearson correlation

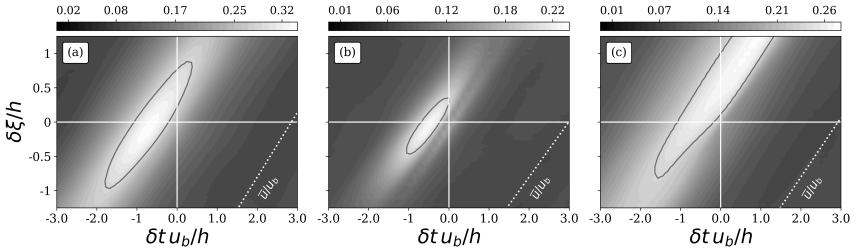


(b) Distance correlation

**Fig. 10**: Space-time correlation (a): $U0T0$, (b): $U1T0$, and (c): $U2T2$ in the streamwise direction evaluated at $x/h \simeq 0$ on the upper solid wall of the periodic hill at $Re_b = 10,595$

### *Correlations* $U0T0$*,* $U1T0$*, and* $U2T2$

Figure 10a (Figure 10b, respectively) shows the Pearson (distance, respectively) correlations $U0T0$, $U1T0$, and $U2T2$ (from left to right) at the separation only. The amplitude for the three Pearson correlations is close to 0.23. For the distance correlation, $U1T0$ and $U2T2$ have approximately the same amplitude, whereas $U0T0$ has a higher amplitude meaning a different probabilistic distribution. The domain of high correlation $\mathcal{D}$ is similar for both types of correlations. In the three cases, the correlation aligns with the mean streamwise velocity $\overline{u}/u_b$ (white dotted line) and is shifted by $-0.5\delta t\, u_b/h$. The correlation $U2T2$ spreads over 2.5 time units in the upper right quadrant (Figure 10ac). This part of the domain cannot be used in the development of a wall model due to causality. Indeed, this part designates the impact of $\tau_{w,z}$ on $u_z$, while the left quadrant indicates the reverse relation: the impact of $u_z$ on $\tau_{w,z}$. One can deduce that $u_z$ is very sensitive to $\tau_{w,z}$. A wrong prediction of $\tau_{w,z}$ can impact the spanwise velocity over 3 space units downstream.

### *Correlations* $P0T0$ *and* $P2T2$

Figure 11 shows the Pearson and distance correlations for $P0T0$ and $P2T2$ in the vicinity of the reattachment point. This location is preferred for illustration as it has the highest correlation value for $P0T0$. Regarding $P2T2$, the

amplitude of the correlations barely varied from one location to another, indicating a weak variation of the spanwise pressure gradient. This observation is also drawn for the distance correlation $P2T2$. For both $P0T0$ and $P2T2$ correlations, the Pearson correlations features an anti-correlation around 15%. The distance correlation indicates the existence of a non-linear relationship between the two variables. Note, however, that the magnitude is different, revealing distinct distributions, whereas Pearson suggests only a weak correlation. The domain $\mathcal{D}$ is much more limited than the one obtained for the correlation with the velocity field. It aligns well with the local mean velocity. Nonetheless, this domain is also slightly shifted downstream ($\delta\xi > 0$) or in the same manner, it observes a time delay; both the time delay and space displacement are negligible here. Hence, one can conclude that instantaneous and local information are enough to characterize the relation between the pressure gradients and the corresponding shear stresses. One notices furthermore that the correlations show some oscillations; these are only observed in the streamwise, not in the spanwise direction as shown in Section 4.2.2.

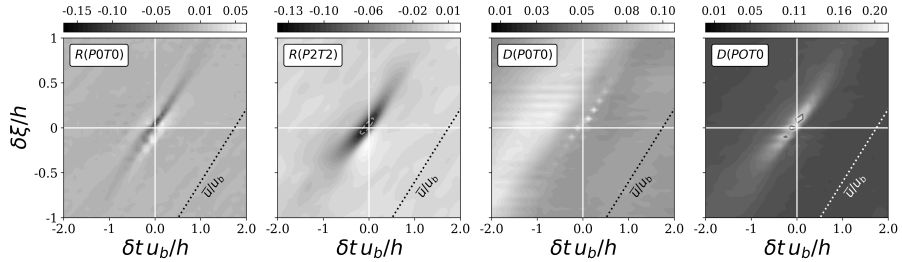


**Fig. 11**: Space-time correlations $P0T0$ and $P2T2$ in the streamwise direction evaluated at $x/h \simeq 4.2$ on the upper wall of the periodic hill at $Re_b = 10,595$

### 4.2.2 Spanwise Pearson correlations

The periodic hill presents a massive separation at $x/h \simeq 0.19$ on the bottom wall. The turbulent free shear layer reattaches on the flat bottom surface at $x/h \simeq 4.21$. At this point, hairpin vortices appear. This phenomenon is three-dimensional, may impact the upper wall, and is quantified with space-time correlations. Five different non-negligible correlations with the velocity field are detected: $U0T0$, $U1T0$, $U0T2$, $U1T2$, and $U2T2$. For the three regions (see Figure 9), the correlations are similar in shape and amplitude, except for the reattachment where a drop of 30% and 50% is measured in the amplitude of the correlation $U1T0$ and $U2T2$, respectively. For this reason, only correlations in the vicinity of the separation region are provided for the sake of brevity. Moreover, distance correlations with the velocity field are not presented because they give a similar domain $\mathcal{D}$ with relevant magnitude evaluated between 15% to 30%. Correlations $U0T0$ and $U1T0$ (Figure 12a and 12b) are similar to

those detected in the channel. At the height of $0.1/h$, compared to the channel, three other correlations are observed: $U1T0$, $U0T2$, and $U2T2$. The two cross-correlations appear as two distinct lobes, one negative and one positive, of equal amplitude, arranged symmetrically around the horizontal axis. Finally, the correlation $U2T2$ is the most remarkable. It has a wide spread in space and time with a non-negligible maximum amplitude of 26%.

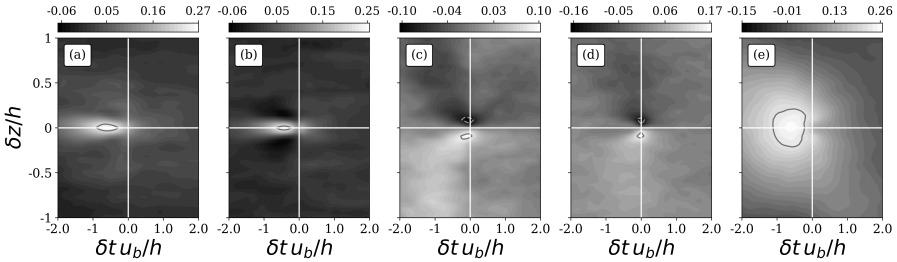


**Fig. 12**: Space-time correlations $U0T0$, $U1T0$, $U0T2$, $U1T2$, and $U2T2$ (from left to right) in the spanwise direction evaluated at $x/h \simeq 9.0$ along the upper wall of the periodic hill at $Re_b = 10,595$

Correlations with pressure gradients are also analyzed in the spanwise direction, and only two correlations are relevant: $P1T2$ and $P2T2$ (not presented here for the sake of brevity and clarity). However, their domain $\mathcal{D}$ is so narrow that instantaneous and local information are perfectly relevant to characterize their relationship with the spanwise wall shear stress.

### 4.2.3 Correlations on the upper wall: conclusion

Although this wall is subject to pressure fluctuations generated by the bottom wall, correlations with the velocity field in the streamwise direction lead to a similar conclusion as for the channel: the peak of high correlation is shifted in $\delta t < 0$ (as emphasized in Figure 3b). If no time delay is considered, a space shift should be taken into account as performed in the shifted boundary condition model of Piomelli *et al.* [34], as already stated for the channel case.

More correlations with the velocity field are detected in the spanwise direction. Similar cross-correlations were also detected on the channel at lower $y^+$ values. As a result of the homogeneity of the spanwise direction, the domain of high correlation $\mathcal{D}$ is always symmetric around the horizontal axis, as expected. One correlation shows a greater extension of the domain $\mathcal{D}$ in the spanwise direction, suggesting an increase in the spanwise stencil used for wall models. This statement is true, if and only if the wall model discretization $(\delta z)_{wmLES}$ is smaller than the spanwise displacement measured with the correlations.

Even though no correlation with the pressure gradient is found for the channel, they are observed for the upper wall of the periodic hill. Due to the massive separation appearing on the bottom wall, the pressure gradient has an

impact on the upper wall. Nonetheless, these correlations are origin-centered and narrow compared to correlations with the velocity field. Hence, instantaneous and local information seems sufficient to characterize the relation with the pressure gradient.

## 4.3 Correlations on the bottom wall of the periodic hill

The shape of the periodic hill leads to separation and reattachment from the curved boundary (see Figure 6). Due to the geometry, the correlation has to be sought at different $x$-region along the bottom wall. Hence, as for the upper wall, distinct regions are targeted: (i) in the vicinity of the separation, (ii) after the reattachment, and (iii) on the convex windward wall of the next hill. These different regions are shown in red in Figure 9. The two first red dots, on the left, are respectively located before and after the averaged separation. The third point is located in the recirculation bubble, while the fourth dot is set just after the averaged reattachment point. The last red square is positioned on the convex windward wall of the next hill, where the flow is subjected to strong acceleration.

### 4.3.1 Streamwise Pearson and distance correlations

The correlations in the streamwise direction are observed at only three locations: $(Sp)$, $(Rt)$, and $(Cwd)$, stating for *separation*, *reattachment* and *convex windward wall of the next hill*, respectively. These three locations correspond to the first red square (starting from the left), the fourth red square, and the last red square in Figure 9, $x/h \simeq 0$, 4.2, 8.0, respectively. Three significant correlations with the velocity field are detected: $U0T0$, $U1T0$, and $U2T2$.

***Correlation*** $U0T0$

For one location (see Figure 13), both the Pearson and the distance correlations present the same domain of high correlation $\mathcal{D}$ but with slightly different amplitude, indicating a non-linear relation between $u_\xi$ and $\tau_{w,\xi}$. Near the separation, the correlations are shifted in the positive $\delta\xi/h$. It means that the separation drives the wall shear stress at $x/h \simeq 0$. One also observes a correlation in the lower left quadrant, implying an impact of the wall curvature located at $x/h \simeq 8.5$ on the wall shear stress at $x/h \simeq 0$. Although the Pearson correlation illustrates an anti-correlation in this lower left quadrant, its magnitude is five times smaller, indicating that the relationship is less strong. However, the distance correlation indicates similar amplitude levels for both domains. One may conclude to take both upstream and downstream information to characterize the relation between $u_\xi$ and $\tau_{w,\xi}$ near separation. None of the lobes align with the local mean velocity. This observation contrasts with our intuition, and more importantly with previous results. The one at $\delta\xi/h = 0.5$ aligns with the horizontal, thus with a zero convection velocity, coherent with the separation phenomenon, whereas the one at $\delta\xi/h = -0.5$ aligns with the mean velocity measured on the convex windward wall of the next hill. For $(Rt)$ and $(Cwd)$,

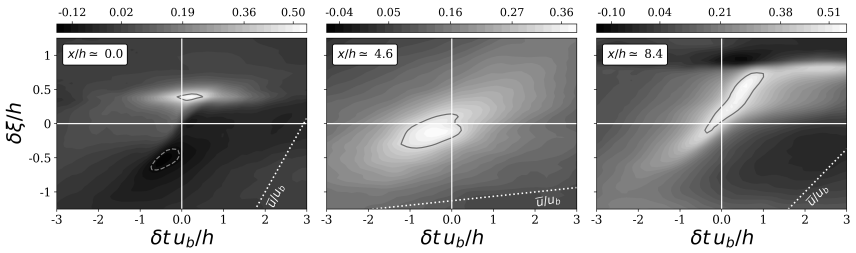


(a) Pearson correlation $U0T0$

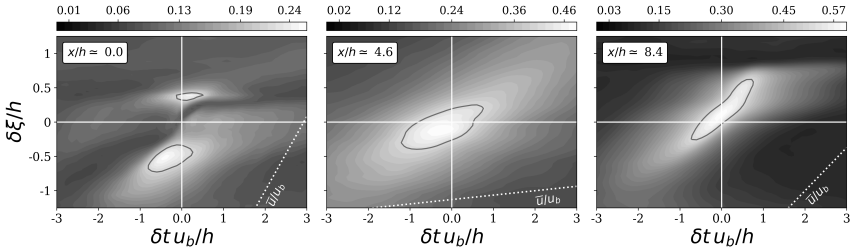


(b) Distance correlation $U0T0$

**Fig. 13**: Space-time correlation $U0T0$ in the streamwise direction evaluated at $x/h \simeq 0, 4.2, 8.0$ (from left to right, corresponding to $Sp$, $Rt$, and $Cwd$) along the lower solid wall of the periodic hill at $Re_b = 10,595$, white dotted line corresponds to $\overline{u}_\xi/u_b$ at a wall-normal distance of $0.1h$

the correlations realign with the local mean velocity. As the velocity increases, the shape of the correlation stretches. Along the convex windward wall of the next hill, the correlation is shifted in $\delta t\, u_b/h > 0$. In this area, it is $\tau_{w,\xi}$ that impacts $u_\xi$, probably due to the curvature effect.

### *Correlation* $U1T0$

The first thing one can notice is the smaller domain of dependence compared to $U0T0$ at each location. As for the channel, the Pearson correlation indicates an anti-correlation between $u_\eta$ and $\tau_{w,\xi}$, still explained by ejection events. Near the separation, the domain of dependence appears to be divided (see Figure 14) into two sub-domains: (a) one at $\delta\xi/h = 0.5$ (like $U0T0$), and (b) one centered on the origin. This (a) sub-domain is less visible on the distance correlation because it has a lower amplitude compared to the (b) sub-domain magnitude. This (b) sub-domain aligns with the local mean velocity while (a) aligns with the horizontal. For ($Rt$) and ($Cwd$), both the Pearson and the distance correlations indicate similar shapes, oriented according to the local mean velocity. The correlations are shifted in $\delta\xi/h < 0$.

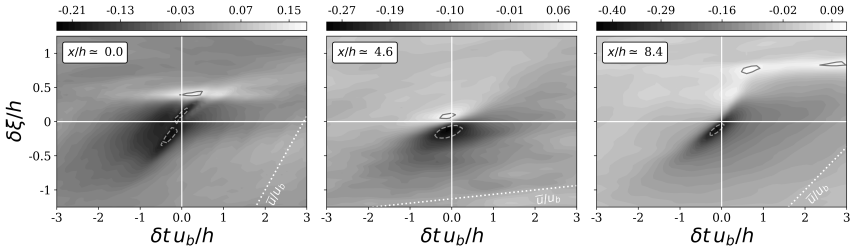


(a) Pearson correlation $U1T0$

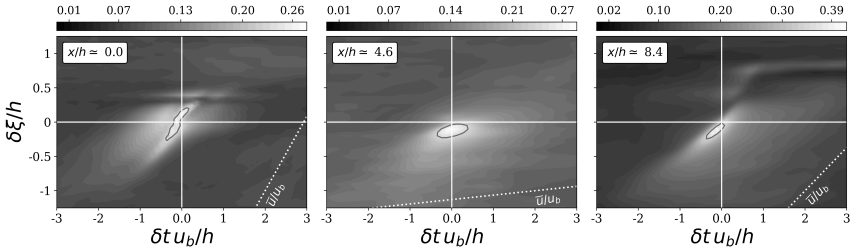


(b) Distance correlation $U1T0$

**Fig. 14**: Space-time correlation $U1T0$ in the streamwise direction evaluated at $x/h \simeq 0$, 4.2, 8.0 (from left to right, corresponding to $Sp$, $Rt$, and $Cwd$) along the lower solid wall of the periodic hill at $Re_b = 10,595$, white dotted line corresponds to $\overline{u}_\xi/u_b$ at a wall-normal distance of 10% of the hill height

### *Correlation* $U2T2$

As for $U0T0$ and $U1T0$, the correlation $U2T2$ (see Figure 15), in the separation vicinity, also appears in two sub-domains: one is located at $\delta\xi u_b/h = 0.5$ and one is located on the lower right quadrant. The Pearson and the distance correlations do not capture the same way this second sub-domain, probably due to a slight statistical convergence issue in capturing this phenomenon. Due to causality, this second sub-domain will be discarded. However, it explains that the $u_z$ on the convex windward wall of the next hill ($\delta\xi/h = -1$) is impacted by $\tau_{w,z}$ near separation over a longer period. Regarding ($Rt$) and ($Cwd$), the correlations do not align with the local mean velocity. They are more tilted, indicating higher convection of the correlated structures.

### *Correlation* $P0T0$

Near the separation, in Figure 16, the domain $\mathcal{D}$ of $P0T0$ appears fragmented, the same way it was for the streamwise correlation for the pressure gradient on the upper wall (see Figure 11). The fragmented domain visible in the lower-left quadrant in the distance correlation is possibly an image of the impact of the pressure gradient on the precursor separation appearing at $x/h \simeq 0$, explained in [6]. While the Pearson correlation indicates a weak anti-correlation, the distance correlation pinpoints a higher value of 21%, indicating a non-linear

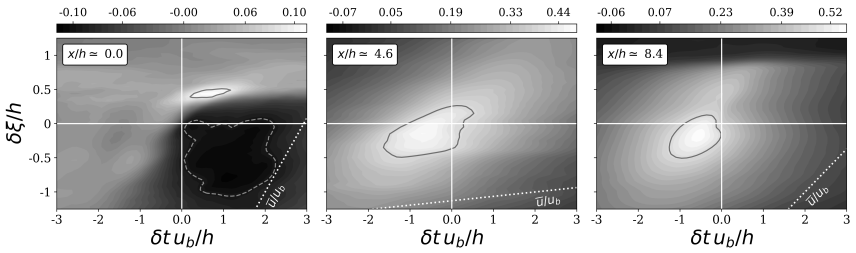


(a) Pearson correlation $U2T2$

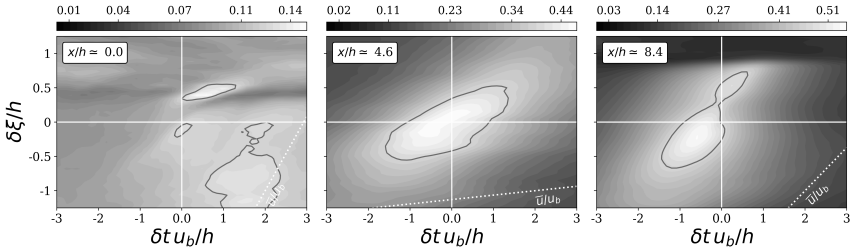


(b) Distance correlation $U2T2$

**Fig. 15**: Space-time correlation $U2T2$ in the streamwise direction, evaluated at $x/h \simeq 0, 4.2, 8.0$ (from left to right, corresponding to $Sp$, $Rt$, and $Cwd$) along the lower solid wall of the periodic hill at $Re_b = 10,595$, white dotted line corresponds to $\overline{u}_\xi/u_b$ at a wall-normal distance of 10% of the hill height

relationship between $\partial p/\partial \xi$ and $\tau_{w,\xi}$. Notice that an increase in the streamwise pressure gradient tends to reduce $\tau_{w,\xi}$ and hence promotes the separation, as expected. This observation is true at each location ($Sp$, $Rt$, and $Cwd$). The correlation aligns with the local mean velocity, except at the separation. At the separation, the correlation aligns with a lower velocity, illustrating the deceleration induced by the separation. The effect of the pressure gradient on $\tau_{w,\xi}$ is even more pronounced when the boundary layer is accelerated on the convex windward wall of the next hill with a value of 30%.

### *Correlation* $P1T0$

A comparable analysis can be drawn for $P1T0$ except at the reattachment where no clear domain of dependence has been detected (see Figure 17). In the vicinity of the separation, the domain of dependence also appears fragmented. It is linked to the oscillatory behavior of the pressure gradient in the streamwise direction, near separation. The distance correlation seems less sensitive to oscillation and detects a correlation shifted in $\delta t > 0$. Another lobe is detected in the lower left quadrant, as for the correlation $U0T0$ and can also explain the precursor separation [6]. In the convex windward wall of the next hill, a positive correlation is observed in contrast to the anti-correlation detected for $P0T0$. Both the Pearson and the distance correlations are shifted in $\delta\xi > 0$.

In the vicinity of the separation, the correlation aligns with a lower velocity as for $P0T0$. Along the convex windward wall of the next hill, the Pearson correlation seems to better capture the alignment with the local mean velocity, while for the distance correlations, the domain $\mathcal{D}$ aligns with a lower velocity.

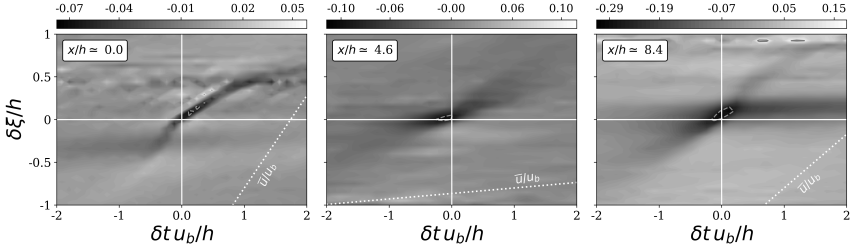


(a) Pearson correlation $P0T0$

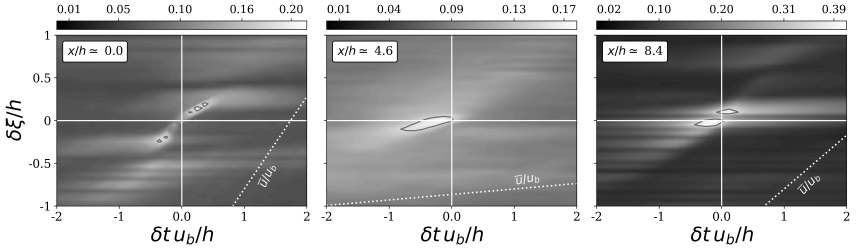


(b) Distance correlation $P0T0$

**Fig. 16**: Space-time correlation $P0T0$ along the streamwise direction, evaluated at $x/h \simeq 0$, 4.2, 8.0 (from left to right, corresponding to $Sp$, $Rt$ and $Cwd$) along the lower solid wall of the periodic hill at $Re_b = 10,595$, white dotted line corresponds to $\overline{u}_\xi/u_b$ at a wall-normal distance of $0.1h$

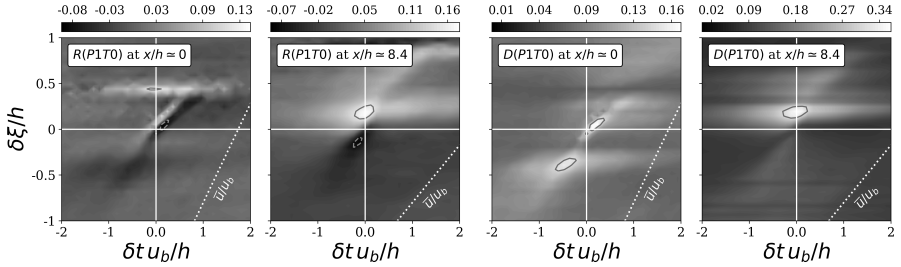


**Fig. 17**: Space-time correlation $P1T0$ along the streamwise direction, evaluated at $x/h \simeq 0$, 8.0 (from left to right, corresponding to $Sp$, $Rt$, and $Cwd$) along the lower solid wall of the periodic hill at $Re_b = 10,595$, white dotted line corresponds to $\overline{u}_\xi/u_b$ at a wall-normal distance of $0.1h$

***Correlation*** *P2T2*

Compared to *P0T0* at the separation, the domain of dependence of *P2T2* (see Figure 18) is less fragmented and spread over time. For the three regions, the correlations (Pearson and distance) are centered at the origin and aligned with the local mean velocity. One can also observe the anti-correlation between $\partial p/\partial z$ and $\tau_{w,z}$ which can be analyzed the same way as *P0T0* and is also coherent with the separation phenomenon in the case of a pressure gradient.

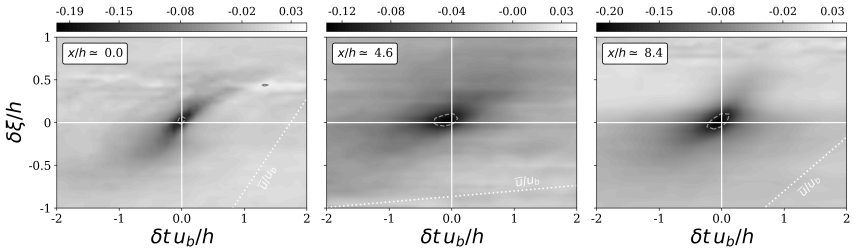


(a) Pearson correlation *P2T2*

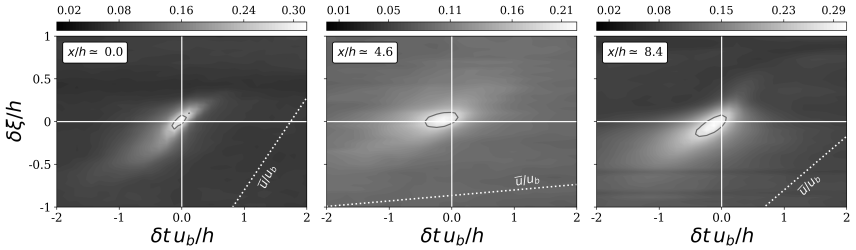


(b) Distance correlation *P2T2*

**Fig. 18**: Space-time correlation *P2T2* along the streamwise direction evaluated at $x/h \simeq 0$, 4.2, 8.0 (from left to right, corresponding to *Sp*, *Rt*, and *Cwd*) along the lower solid wall of the periodic hill at $Re_b = 10,595$, white dotted line corresponds to $\overline{u}_\xi/u_b$ at a wall-normal distance of $0.1h$

### 4.3.2 Spanwise Pearson correlations

This wall presents, as already stated, a massive separation followed by a reattachment on the flat bottom part at $x/h \simeq 4.2$. Although the flow is on average two-dimensional, turbulence and these two phenomena are three-dimensional, requiring an analysis of spanwise correlations. However, correlations observed in that direction are not radically different from those observed on the channel and the upper wall. It can be concluded that the streamwise direction is the driving direction for these three configurations. A few existing wall models using instantaneous and local velocity sometimes account for the spanwise

direction by averaging data along that direction. Nonetheless, they fail to predict the wall shear stress for such a wall, which reinforces the interest in the streamwise direction than the spanwise one.

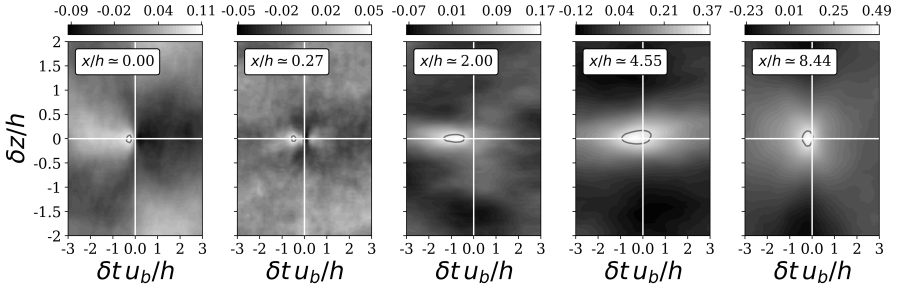


**Fig. 19**: Pearson space-time correlation $U0T0$ along the spanwise direction, measured at five locations (Fig.9) along the bottom wall of the periodic hill at $Re_b = 10,595$

Unlike spanwise correlations measured for the upper wall, these correlations are different in both shape and amplitude for the five regions (see red squares in Figure 9). Nonetheless, they behave the same way. For the correlations $U0T0$, $U1T0$, and $U2T2$ (where $U0T0$ is displayed in Figure 19), the domain of high correlation $\mathcal{D}$ is centered around the horizontal axis and slightly shifted in the $\delta t < 0$. For the correlations $U2T0$, $U0T2$, and $U1T2$, the domain $\mathcal{D}$ is split into two sub-domains, one of negative amplitude and one of positive and equal amplitude. Only the correlation U2T0 is shown in Figure 20. Note how these negative and positive sub-domains are inverted in the recirculation bubble. In contrast to the upper wall, the spanwise extent of the domain $\mathcal{D}$ is greater. All these correlations are, as expected, symmetric about the horizontal axis. Some of them are not perfectly symmetrical due to a lack of statistical convergence. We note that the correlations $U2T0$ reach relatively important values near the reattachment region ($x/h = 4.55$) and hill crest ($x/h = 8.44$).

### 4.3.3 Correlations on the lower wall: conclusion

The major difference compared to streamwise correlations obtained on the upper wall is the dipole detected in the vicinity of the separation for every correlation with the velocity field. This behavior is not always reflected in the correlation with the pressure gradient. All correlations are even more position-dependent along the bottom wall, while those of the top wall were insensitive to position, explained by the low impact of the bottom wall on the top one. However, for attached flows, correlations look like those observed on the channel flow.

The behavior of the spanwise correlations is comparable to those observed on the upper wall and those for the channel at lower $y+$. The correlations also

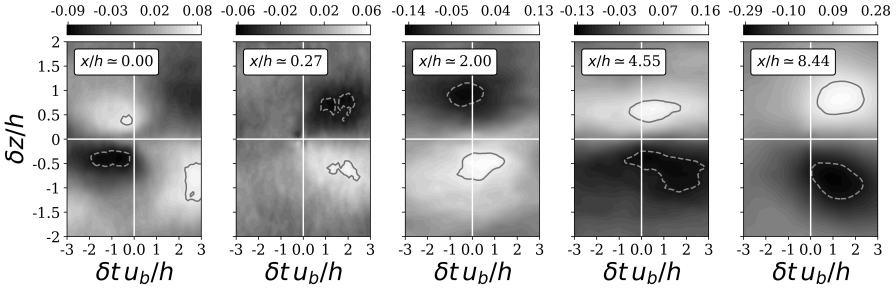


**Fig. 20**: Pearson correlation $U2T0$ in the spanwise direction, measured at five locations (Fig.9) along the bottom wall of the periodic hill at $Re_b = 10,595$

appear in one or two lobes which are symmetric about the horizontal axis, reflecting the absence of convection in the spanwise direction. However, the domain of dependence is more widely spread in the spanwise direction, with significant values up to $\delta z/h \simeq \pm 1$. This observation suggests the interest in the enlargement of the domain of dependence in the z-direction for wall models applied to reattachment phenomena. Moreover, a correlation of 30% between the spanwise velocity and the streamwise wall shear stress indicates 3D effects and non-negligible coupling in the wall-parallel direction.

# 5 Conclusion

The present study addresses the analysis of near-wall physics in equilibrium and non-equilibrium flow conditions. Such an analysis is performed using space-time correlations. These correlations aim to find functional relations between volume quantities and the wall shear stress for various configurations, covering the simple channel flow to separating and reattaching flow. Two types of correlations (i.e., the Pearson and the distance) have been used to better understand the physics that develops on each flow configuration.

On a channel flow, the wall shear stress is mainly driven by the streamwise velocity components and no correlation with the pressure gradient has been found in the logarithmic layer as also stated by Abel *et al.* [1]. The obtained correlations have an elongated elliptical shape that extends over about $200\delta t^+$. To compensate for this delay, a downstream displacement can be considered as proposed in the work of Piomelli *et al.* [34] for their shifted boundary condition model. At lower $y^+$ values (i.e., $y^+ < 100$), significant cross-correlations in the z-direction are noticed. However, they were no longer relevant at $y^+ \geq 100$ values except the $U0T0$ and $U2T2$. One may conclude that at higher wall-normal distances, three-dimensional effects generated by the wall are reduced.

Regarding the periodic hill flow, we subdivided the analysis into the upper and lower wall. On the upper wall, similar correlations compared to those observed on the channel are obtained. Although the streamwise direction is not

homogeneous, all detected correlations are found independent of the streamwise position, meaning that the lower wall has a minor impact on the upper one. Unlike the channel, correlations with the pressure gradient are found, above the reattachment region on the upper wall, in the streamwise and the spanwise direction, revealing at least an impact on the flow physics of the lower wall on the upper wall. Major differences are noticed for the lower wall, where distinct correlations are obtained for the separation, reattachment, and the convex windward wall of the next hill. The reattachment and converging regions behave similarly to a channel wall except that correlations are less spread in time and thicker. More relevant correlations with the pressure gradient are collected as an image of the impact of the pressure gradient on the separation and reattachment phenomena. Oscillatory behavior is only detected near separation, whereas on the upper wall it is observed at every streamwise location. The most interesting behavior is obtained in the vicinity of the separation. There, the correlation is divided into two sub-domains. One of them is shifted to $\delta\xi > 0$, indicating that the formation of the recirculation bubble has a strong (and non-linear) impact on the separation point. The second sub-domain reveals an anti-correlation located on the convex windward wall of the next hill on the separation point. In the spanwise direction, despite the homogeneity of the flow, significant correlations are nevertheless found in some locations. These correlations look like those obtained on the channel flow at lower $y^+$ values. However, for the cross-correlations, the change in sign of the lobes depends on the position along the bottom wall (i.e., inside or outside the bubble).

Since this work tackles non-equilibrium conditions, the conclusion drawn may not apply to other flow configurations. However, this study is a preliminary step for the development of a data-driven wall model applied to the separation phenomenon on the two-dimensional periodic hill. Under these assumptions, the following rules can be applied. These correlations mainly provide information on the stencil to be used as inputs for a data-driven wall model. The stencil refers to the number of streamwise and/or spanwise positions to consider as well as the time delay to account for. As already stated, existing wall models accounting for the instantaneous and local velocity predict correctly the wall shear stress on the channel and the upper wall [19, 20]. Nonetheless, correlations on the channel show that as moving away from the wall, the domain of high correlation $\mathcal{D}$ is shifted in the $\delta t^+ < 0$. This time delay is strongly dependent on the wall-normal height at which the information is sought. It can be argued that there is a wall-normal distance below which this time delay is invisible (i.e., too small to be of interest to wmLES). Above this height, a small-time delay (past times) or a space displacement (downstream) has to be accounted for to correctly capture the high correlation between the wall shear stress and the velocity. The correlations in the spanwise direction undergo the same treatment, except that there is no convection along this direction. Hence only a time delay can improve the model. This delay also depends on the wall-normal height. A similar conclusion can be drawn for the

upper wall of the periodic hill, except that the relationship between the volume fields and the wall shear stress can be enriched if the pressure gradient is considered. Note that in this case, the spanwise domain may also be expanded due to the correlation between $u_z$ and $\tau_{w,z}$ that appears as two symmetrical lobes. On the lower wall, near the reattachment, and on the convex windward wall of the next hill, almost all correlations in the streamwise direction are shifted in space and time. The time delay and the space displacement are linked to the local mean velocity. However, in the vicinity of the separation, the correlations split into two lobes, and none of them aligns with the local mean velocity. The lobe shifted in $\delta\xi > 0$ aligns with the horizontal, indicating the impact of the recirculation bubble, which can be considered as a dead zone. The other lobe is shifted in the $\delta\xi < 0$ and aligns with the local mean velocity measured on the convex windward wall of the next hill. In these non-equilibrium conditions, local and instantaneous information may not be enough to characterize a separated flow. For this configuration at $Re_b = 10,595$, a space displacement $\delta\xi/h$ of 0.5, up and downstream, is required to fully characterize the relationship with the velocity field. In addition to this streamwise displacement, a spanwise displacement is also required to capture the two lobes of cross-correlations. If causality is respected, a displacement $\delta z/h$ of 0.5 (left and right) is needed. If the time delay is not considered, the input of the wall model can be seen as a two-dimensional image of the velocity and pressure gradients.

This work can be extended to other non-equilibrium configuration such as the Backward Facing Step, for which the flow separates due to a discontinuity in the geometry. It should be also noted that the present work only covered 3D-extruded configurations. In those configurations, the wall-parallel directions are well defined (i.e., streamwise and spanwise direction). Moreover, correlations show how the streamwise direction prevails over the spanwise one; although the latter can still be important in some configurations. In the case of more complex 3D configurations presenting skewed boundary layers, the wall-parallel directions do furthermore not necessarily coincide with the streamwise and spanwise directions. A future work could be the analysis wall-parallel space-time correlations of a complex 3D configuration.

**Acknowledgments.** The present research benefited from computational resources made available on the Tier-1 supercomputer of the Fédération Wallonie-Bruxelles, infrastructure funded by the Walloon Region under the grant agreement n°1117545. The funding of M. Boxho by Safran Tech is gratefully acknowledged.

## ETHICAL STATEMENT.

- Funding: Safran Tech and computational resources made available on the Tier-1 supercomputer of the Fédération Wallonie-Bruxelles, infrastructure funded by the Walloon Region under the grant agreement n°1117545.
- Conflict of interest/Competing interests: Not applicable
- Ethics approval: Not applicable
- Consent to participate: Not applicable

- Consent for publication: Not applicable
- Availability of data and materials: No but can be made available if needed
- Code availability: No but can be made available if needed

# References

[1] Abel, M., Stojkovic, D., Breuer, M.: Nonlinear stochastic estimation of wall models for LES. Heat and Fluid Flow. 27(2), 267-278 (2006). https://doi.org/10.1016/j.ijheatfluidflow.2005.10.011

[2] Balaras, E., Benocci, C., and Piomelli, U.: Two-layer approximate boundary conditions for large-eddy simulations. AIAA J. 34(6), 1111–1119 (1996). https://doi.org/10.2514/3.13200

[3] Benocci, C., & Pinelli A.: The role of the forcing term in the large-eddy simulation of equilibrium channel flow. In Engineering Turbulence Modeling and Experiments. Elsevier, 287-296 (1990).

[4] Bose, S. T. and Park, G. I.: Wall-modeled large-eddy simulation for complex turbulent flows. Annual Review of Fluid Mechanics. 50, 535-561 (2018). https://doi.org/10.1146/annurev-fluid-122316-045241

[5] Breuer, M., Peller, N., Rapp, Ch., Manhart, M.: Flow over Periodic Hills - Numerical and Experimental Study in a Wide Range of Reynolds Numbers. Computers & Fluids. 38(2), 433-457 (2009). https://doi.org/10.1016/j.compfluid.2008.05.002

[6] Breuer, M., Kniazev, B., Abel, M.: Development of wall models for LES of separated flows using statistical evaluations. Computers & Fluids 36(5), 817-837 (2007). https://doi.org/10.1016/j.compfluid.2006.09.001

[7] Brunton, S. L., Noack, B. R., and Koumoutsakos, P.: Machine learning for fluid mechanics. Annual Review of Fluid Mechanics. 52, 477–508 (2020). https://doi.org/10.1146/annurev-fluid-010719-060214

[8] Cadieux, F., Sadique, J., Yang, X. I., Meneveau, C., & Mittal, R.: Wall-modeled large eddy simulation of laminar and turbulent separation bubble flows. In 46th AIAA fluid dynamics conference. AIAA 2016-3189. (2016). https://doi.org/10.2514/6.2016-3189

[9] Carton de Wiart, C., Hillewaert, K., Bricteux, L., & Winckelmans, G.: LES using a Discontinuous Galerkin method: Isotropic turbulence, channel flow and periodic hill flow. In: Fröhlich, J., Kuerten, H., Geurts, B., Armenio, V. (eds) Direct and Large-Eddy Simulation IX. ERCOFTAC Series, vol 20. Springer, Cham. (2015). https://doi.org/10.1007/978-3-319-14448-1_13

[10] Carton de Wiart, C., Hillewaert, K., Bricteux, L., and Winckelmans, G.: Implicit LES of free and wall bounded turbulent flows based on the discontinuous Galerkin/symmetric interior penalty method. International Journal of Numerical Methods in Fluids. 78(6), 335–354 (2014).

[11] Chaudhuri, A. and Hu, W.: A fast algorithm for computing distance correlation. Computational Statistics & Data Analysis. 135, 15-24 (2019). https://doi.org/10.1016/j.csda.2019.01.016.

[12] Cheng, C., Li, W., Lozano-Duran A. and Liu H.: On the structure of streamwise wall-shear stress fluctuations in turbulent channel flows. Journal of Fluid Mechanics. 903, A29 (2020). https://doi.org/10.1017/jfm.2020.639

[13] Colella, K. J., & Keith, W. L.: Measurements and scaling of wall shear stress fluctuations. Experiments in Fluids 34, 253–260 (2003). https://doi.org/10.1007/s00348-002-0552-2

[14] Dawson, S. T. M. and McKeon, B. J.: On the shape of resolvent modes in wall-bounded turbulence. J. Fluid Mech., 877, 682-716 (2019). https://doi.org/10.1017/jfm.2019.594

[15] Deardoff, J. W.: A numerical study of three-dimensional turbulence channel flow at large Reynolds numbers. Journal of Fluid Mechanics. 41(2), 453-480 (1970). https://doi.org/10.1017/S0022112070000691

[16] Duraisamy, K., Iaccarino, G., and Xiao, H.: Turbulence modeling in the age of data. Annual Review of Fluid Mechanics. 51, 357–377 (2019).

[17] Edelmann, D., Mori, T. F., & Székely, G. J.: On relationships between the Pearson and the distance correlation coefficients. Statistics & Probability Letters. 169, 108960 (2021). https://doi.org/10.1016/j.spl.2020.108960

[18] Frère, A.: Towards wall-modeled Large-Eddy Simulations of high Reynolds number airfoils using a Discontinuous Galerkin method (Unpublished doctoral dissertation). Université catholique de Louvain. (2018).

[19] Frère, A., Carton de Wiart, C., Hillewaert, K., Chatelain, P., & Winckelmans, G.: Application of wall-models to Discontinuous Galerkin LES channel flow. Physics of Fluids. 9(8), 085111 (2017). https://doi.org/10.1063/1.4998977

[20] Frère, A., Hillewaert, K., Chatelain, P., & Winckelmans, G.: High Reynolds number airfoil: from wall-resolved to wall-modeled LES. Flow, Turbulence and Combustion. 101, 457–476 (2018).

[21] Fröhlich, J., Mellen, C. P., Rodi, W., Temmerman, L., & Leschziner, M. A.: Highly resolved large-eddy simulation of separated flow in a channel with streamwise periodic constrictions. Journal of Fluid Mechanics. 526, 19–66 (2005). https://doi.org/10.1017/S0022112004002812

[22] Gloerfelt X., & Cinnella P.: Investigation of the flow dynamics in a channel constricted by periodic hills. 45th AIAA Fluid Dynamics Conference. Dallas. United States. 2015-2480 (2015). https://doi.org/10.2514/6.2015-2480

[23] Grötzbach, G. in Encyclopedia of Fluid Mechanics, edited by N. P. Cheremisinoff (Gulf, West Orange, NJ, 1987), Vol. 6., (1987).

[24] Hoffmann G., Benocci C.: Approximate wall boundary conditions for large eddy simulations. In: Benzi, R. (eds) Advances in Turbulence V. Fluid Mechanics and Its Applications, vol 24. Springer, Dordrecht (1995). https://doi.org/10.1007/978-94-011-0457-9_40

[25] Hornik, K.: Approximation capabilities of multilayer feedforward networks. Neural Networks. 4(2), 251–257 (1991). https://doi.org/10.1016/0893-6080(91)90009-T

[26] Hoyas, S. and Jimenez, J.: Reynolds number effects on the Reynolds-stress budgets in turbulent channels. Physics of Fluids. 20, 101511 (2008). https://doi.org/10.1063/1.3005862

[27] Hillewaert, K.: Development of the Discontinuous Galerkin method for high-resolution, large scale CFD and acoustics in industrial geometries. PhD thesis. Ecole polytechnique de Louvain/iMMC (February 2013).

[28] Krank, B., Kronbichler, M., & Wall, W. A.: A multiscale approach to hybrid RANS/LES wall modeling within a high-order Discontinuous Galerkin scheme using function enrichment. Numerical Methods in Fluids. 90(2), 81–113 (2019). https://doi.org/10.1002/fld.4712

[29] Lozano-Durán, A. and Bae, H. J.: Self-critical machine-learning wall-modeled LES for external aerodynamics. arXiv:2012.10005 [physics] (2021). http://arxiv.org/abs/2012.10005.

[30] Marusic, I. and Monty, J. P.: Attached Eddy Model of Wall Turbulence. Annual Review of Fluid Mechanics. 51, 49-74 (2019). https://doi.org/10.1146/annurev-fluid-010518-040427

[31] Mason, P. J., Callen, N. S.: On the magnitude of the subgrid-scale eddy coefficient in large eddy simulation of turbulent channel flow, Journal of Fluid Mechanics. 162, 439-462 (1986). https://doi.org/10.1017/S0022112086002112

[32] McKeon, B. J.: The engine behind (wall) turbulence: perspectives on scale interactions, Journal of Fluid Mechanics. 817, (2017). https://doi.org/10.1017/jfm.2017.115

[33] Nicoud, F., Baggett, J. S., Moin, P., and Cabot, W.: Large eddy simulation wall-modeling based on suboptimal control theory and linear stochastic estimation. Physics of Fluids. 13, 2968 (2001). https://doi.org/10.1063/1.1389286

[34] Piomelli, U., Moin, P., Ferziger, J. H. and Kim, J.: New approximate boundary conditions for large-eddy simulations of wall-bounded flows. Physics of Fluids A: Fluid Dynamics 1, 1061 (1989). https://doi.org/10.1063/1.857397

[35] Piomelli, U., Balaras, E.: Wall-Layer Models For large Eddy Simulations. Annual Review of Fluid Mechanics. 34, 349-374 (2002). https://doi.org/10.1146/annurev.fluid.34.082901.144919

[36] Piomelli, U., Wall-layer models for large-eddy simulations. Progress in Aerospace Sciences. 44(6), 437-446 (2008). https://doi.org/10.1016/j.paerosci.2008.06.001

[37] Rajagopalan, S. and Antonia, R. A.: Some properties of the large structure in a fully developed turbulent duct flow. The Physics of Fluids. 22, 614 (1979). https://doi.org/10.1063/1.862643

[38] Song, S., & Eaton, J.: Flow structures of a separating, reattaching, and recovering boundary layer for a large range of Reynolds number. Experiments in Fluids. 36, 642–653 (2004). https://doi.org/10.1007/s00348-003-0762-2

[39] Spalart, P. R., Jou W. H., Strelets M., Allmaras S. R.: Comments on the feasibility of LES for wings and on a hybrid RANS/LES approach. Advances in DNS/LES: Direct numerical simulation and large eddy simulation, 137-148 (1997).

[40] Schumann, U.: Subgrid-scale model for finite-difference simulations of turbulent flows in plane channels and annuli. Journal of Computational Physics. 18(4), 376-404 (1975). https://doi.org/10.1016/0021-9991(75)90093-5

[41] Székely, G. J., Rizzo, M. L., & Bakirov, N. K.: Measuring and testing dependence by correlation of distances. The Annals of Statistics. 35(6), 2769–2794 (2007). https://doi.org/10.1214/009053607000000505

[42] Temmerman, L., Leschziner, M., Mellen, C., & Fröhlich, J.: Investigation of subgrid-scale models and wall-function approximations in large eddy

simulation of separated flow in a channel with streamwise periodic constrictions. International Journal of Heat and Fluid Flow. 24(2), 157–180 (2003). https://doi.org/10.1016/S0142-727X(02)00222-9

[43] Townsend, A.A.: The structure of turbulent boundary layer. Math. Proc. Camb. Philos. Soc. 47, 375-95. (1951).

[44] Townsend, A.A.: The structure of turbulent shear flows, Cambridge, UK: Cambridge Univ. Press. (1961).

[45] Townsend, A.A.: The structure of turbulent shear flows, Cambridge, UK: Cambridge Univ. Press 2nd ed. (1976).

[46] Wang, M.: LES with wall models for trailing-edge aeroacoustics. In Annu Res. Briefs. Center Turbul. Res. Stanford Univ. Calif. 355-364 (1999).

[47] Werner, H., Wengle, H.: Large-eddy simulation of turbulent flow around a cube in a plane channel. In Selected Papers from the 8th Symposium on Turbulent Shear Flows, ed. F. Durst, F., Friedrich, R., Launder, B. E., Schumann, U., Whitelaw, J. H., New York: Springer. 155-168 (1993).

[48] Yang, X. I. A., Zafar S., Wang J.-X., and Xiao H.: Predictive large-eddy-simulation wall modeling via physics-informed neural networks. Physical Review Fluids. 4, 034602 (2019). https://doi.org/10.1103/PhysRevFluids.4.034602

[49] Zhou, Z., He, G., and Yang X.: Wall model based on neural networks for LES of turbulent flows over periodic hills. Physical Review Fluids. 6, 054610 (2021). https://doi.org/10.1103/PhysRevFluids.6.054610